

Frosting Image Recognition detection for R290 Secondary Loop Air Conditioning Heat Pump Systems in Electric Vehicles

Panlin Gu¹, Kang Li^{1*}, Jingxuan Xu¹, Zilong Wang¹, Jinjun Yan², Liaokuo Song², Qize He³, Chao Li⁴, Soheil Mohtaram¹

¹ School of Energy and Power Engineering, University of Shanghai for Science and Technology, Shanghai 200093, China

² China Three Gorges Renewables (Group) Co., Ltd., Beijing, 100032, China

³ Shanghai Fire Research Institute of MEM, Shanghai 200032, China

⁴ Investigation, Design & Research Institute Co., Ltd, Shanghai 200080, China

(Corresponding Author: lklk789@usst.edu.cn Kang Li)

ABSTRACT

R290 secondary-loop air conditioning heat pump systems are a promising alternative for electric vehicles due to their environmental friendliness and high thermal efficiency. At ambient temperatures around 0°C, heat exchangers are prone to frosting, which reduces heating performance; rapid frost detection can significantly enhance system efficiency. In this study, a deep learning-based image recognition method was developed for frost detection in R290 heat pump systems. Experiments were conducted to observe the frosting process and obtain heat transfer characteristics. The results indicate that frosting can be divided into three stages: a sharp decline in the initial stage, a stable development stage, and a rapid decrease during the frosting stage. A modified deep learning approach was used to detect these stages, achieving over 95% accuracy across different temperatures after 150 training rounds. These results demonstrate that the method is reliable and effective under varying conditions.

Keywords: R290, air conditioning heat pump system, defrosting, image recognition

NONMENCLATURE

Abbreviations

| | |
|------------|------------------------------------|
| LLPHE | Liquid-liquid plate heat exchanger |
| VLPHE | Vapor-liquid plate heat exchanger |
| VL Sep | Vapor -liquid separator |
| Outdoor HX | Outdoor Heat Exchanger |
| EEV | Electronic expansion valve |
| EV | Electric vehicle |

Symbols

| | |
|-----|--------------------------------|
| COP | Coefficient of performance [/] |
| FCR | Frost coverage rate [%] |

| | |
|--------|--|
| c | Specific heat capacity of refrigerant [J/(kg.K)] |
| ρ | Density of refrigerant [kg/m ³] |
| VR | Cold flow rate of refrigerant [Kg/h] |
| TLLi | Inlet temperature of liquid-liquid plate heat exchanger [C] |
| TLLo | Outlet temperature of liquid-liquid plate heat exchanger [C] |
| QR | Refrigerating capacity [J] |
| VH | Heat flow rate of refrigerant [Kg/h] |
| TVLi | Inlet temperature of Vapor -liquid plate heat exchanger [C] |
| TVLo | Outlet temperature of Vapor -liquid plate heat exchanger [C] |
| QH | Heating capacity [J] |
| W | Compressor power [W] |

1. INTRODUCTION¹

The secondary-circuit heat pump system using the natural refrigerant R290 (propane) [2], valued for its environmental friendliness and high efficiency [1], shows significant potential for electric vehicle thermal management. However, when operating in low-temperature, high-humidity environments, the surface temperature of the outdoor heat exchanger can fall below the dew point, causing water vapor to condense into a frost layer upon contact [3]. This frost formation reduces heat exchange efficiency. Therefore, timely and accurate detection of frost onset is essential to ensure efficient system operation under low-temperature conditions.

Frost detection is a critical step in the defrosting process [7,8]. Conventional methods for heat pump air conditioning systems typically rely on changes in evaporator temperature sensors, using temperature thresholds to determine whether defrosting is required.

However, this approach is susceptible to external environmental factors, such as outdoor temperature and humidity. In recent years, intelligent algorithms have been widely applied in various fields. Researchers have proposed numerous methods based on such algorithms, including neural network models [4,5] and image recognition techniques [6]. These methods, through real-time monitoring of frost layer thickness and the application of data-driven algorithms, can determine the optimal timing and strategy for initiating defrosting.

As discussed, deep learning-based image recognition offers high intelligence and accuracy. Moreover, incorporating an attention mechanism can further optimize the model, enhancing the accuracy of frosting and defrosting judgment. Therefore, this paper proposes a method for frosting and defrosting determination in the secondary circuit of an R290 heat pump air conditioning system, based on image recognition with an attention mechanism. Different defrosting modes are applied according to the judgment results [9,10]. The remainder of this paper is organized as follows: Section 2 describes the system principles under different modes and the experimental setup; Section 3 presents the results and discussion; and Section 4 summarizes the main conclusions.

2. EXPERIMENTAL SETUP

2.1 R290 secondary loop heat pump air conditioning system

This section provides a detailed explanation of the EV thermal management system using R290 refrigerant, including its working modes. The R290 system refrigerant circuit consists of four core components: a compressor, an expansion valve, a vapor–liquid plate heat exchanger (VLPHE), and a liquid–liquid plate heat exchanger (LLPHE). The system is equipped with a vapor–liquid separator (VL sep) to prevent liquid slugging in the compressor and to enable real-time monitoring of the refrigerant flow state. Heat exchange between the refrigerant circuit (primary loop) and the coolant circuit (secondary loop) is achieved through the two plate heat exchangers, VLPHE and LLPHE.

As shown in Figure 1, when the system operates in heating mode, valves 3, 5, 6, 7, 11, 12, and 14 are open, while valves 1, 2, 4, 8, 9, 10, and 13 are closed. In the primary loop, the high-temperature, high-pressure gaseous refrigerant exits the compressor and releases heat in the VLPHE (acting as a condenser), transforming into a medium-temperature, high-pressure liquid. It then

passes through the electronic expansion valve (EEV), becoming a low-temperature, low-pressure mist-like

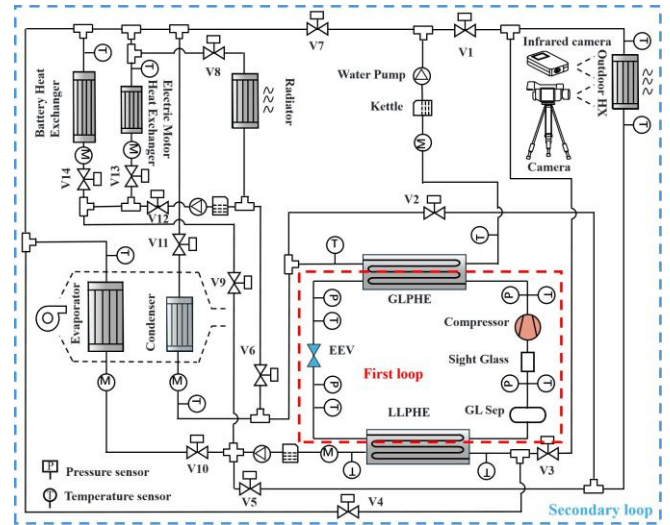


Fig. 1 System Schematic Diagram

working fluid. Finally, it absorbs heat in the LLPHE (acting as an evaporator) and returns to the compressor as a low-temperature, low-pressure superheated vapor via the VL sep.

In the secondary loop, the coolant absorbs heat released by the refrigerant in the VLPHE, which is used to warm the passenger cabin (condenser) and the battery heat exchanger. The coolant then transfers its thermal energy to the refrigerant in the LLPHE, and the resulting cooling capacity is dissipated through the outdoor heat

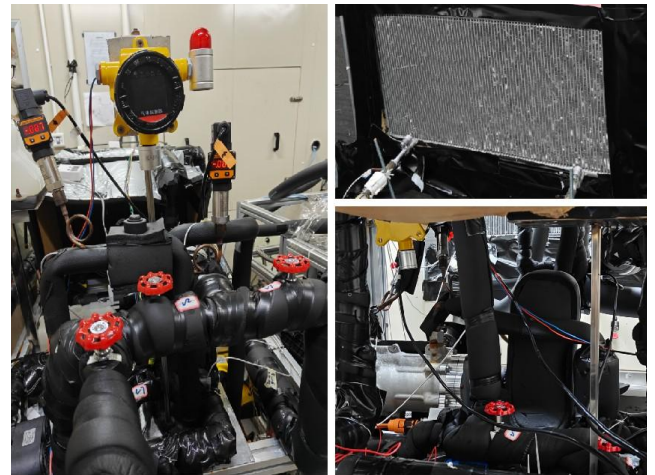


Fig. 2 Physical object image

exchanger (Outdoor HX).

Figure 2 shows the physical setup used in this study. All experimental equipment was arranged outside the environmental chamber and operated in a full fresh-air circulation mode. In the coolant measurement system, temperature sensors were installed at the inlet and

outlet of each heat exchanger to monitor the temperature changes of the fluid after passing through the exchangers. Due to equipment limitations, no flow measurement device was installed for the refrigerant; instead, the heat exchange capacity was calculated based on the coolant temperature measurements. The outdoor heat exchanger is located in the upper left corner of the setup.

2.2 Experimental operating conditions and calculation formulas

The operating ambient temperature of heat pump air conditioning systems in winter typically ranges from $-5\text{ }^{\circ}\text{C}$ to $5\text{ }^{\circ}\text{C}$. Selecting $0\text{ }^{\circ}\text{C}$, $2\text{ }^{\circ}\text{C}$, and $-2\text{ }^{\circ}\text{C}$ covers this core range, making the experimental results more representative of real-world frost-related issues and enhancing the practical relevance of the study. Speeds of 4000 rpm and 5000 rpm correspond to typical operating conditions for heat pump air conditioning systems, particularly in electric vehicles. The working conditions used in this study are summarized in Table 1.

Table 1. Working conditions

| Parameters | condition |
|--|------------|
| Ambient temperature ($^{\circ}\text{C}$) | 2, 0, -2 |
| Compressor speed (rpm) | 4000, 5000 |

Uncertainty analysis is an essential component to ensure the scientific validity, reliability, and practical relevance of the research. The uncertainty statistics for this study are summarized in Table 2.

Table 2. Uncertainty analysis

| Measurement parameters | Uncertainty |
|---|--------------|
| Refrigerant-side temperature ($^{\circ}\text{C}$) | ± 0.1 |
| Refrigerant-side pressure (MPa) | ± 0.0046 |
| Coolant-side temperature ($^{\circ}\text{C}$) | ± 0.2 |
| Refrigerant-side volumetric flow rate (L/min) | ± 0.003 |
| Fan airflow rate (m^3/h) | ± 0.01 |
| Air-side temperature ($^{\circ}\text{C}$) | ± 0.1 |
| Air-side relative humidity (%) | ± 0.5 |
| Coolant-side heat transfer rate (W) | 3.8% |
| Air-side heat transfer rate (W) | 4.1% |
| Compressor power (W) | 2.8% |
| Coefficient of Performance | 3.6% |

This study employed a dual-mode image acquisition system to simultaneously record the frost morphology and temperature distribution on the surface of the outdoor heat exchanger. The system was positioned approximately 0.5 m in front of the heat exchanger to

ensure full coverage of the entire surface. The two cameras were triggered synchronously, continuously collecting data throughout the entire frosting cycle. Temperature mapping was implemented using Python and MATLAB, with MATLAB handling the calibration between grayscale values and temperature.

Under the system operating mode, the heating and cooling capacities serve as key indicators for evaluating overall system performance, requiring a comprehensive assessment of the operating conditions. These capacities can be calculated using Eqs. (1) and (2). This study employed a dual-mode image as follows:

$$Q_R = \frac{C_R \rho_R V_R \Delta T_R}{60} \quad (1)$$

$$Q_H = \frac{C_H \rho_H V_H \Delta T_H}{60} \quad (2)$$

The coefficient of performance (COP) of the heat pump system is determined by Eq. (3).

$$COP = \frac{Q_H}{W} \quad (3)$$

This paper introduces the Frost Coverage Rate (FCR) as a metric to characterize the frosting behavior of the outdoor heat exchanger under different operating conditions. FCR also enables analysis of system performance trends corresponding to varying frost levels. The formula for calculating the Frost Coverage Rate is presented below:

$$FCR = \frac{A_{frost}}{A} \quad (4)$$

In the formula, A_{frost} represents the frosted area on the heat exchanger surface, and A denotes the total surface area of the outdoor heat exchanger. Based on the Frost Coverage Rate (FCR) concept, image processing was performed using MATLAB to calculate the frosted area, enabling the determination of the FCR value.

2.3 Image recognition principle

Figure 3 illustrates the flowchart of the deep learning-based frost detection algorithm proposed in this study, including the core network architecture and a schematic of the camera positioning. The algorithm begins by loading preprocessed infrared image data into a pre-trained ResNet50 model. This model employs residual connections, enabling the training of deeper networks. During training, a spatial attention module is integrated, generating spatial weights through global max pooling and average pooling operations on the feature maps. This enhances the model's focus on critical regions of the frost layer. The algorithm also

incorporates branching logic that dynamically adjusts the training path based on data augmentation strategies. Finally, the process outputs classification results from the ResNet50 model enhanced with the attention mechanism.

The left side of the flowchart illustrates the core residual learning unit of ResNet50, which facilitates effective gradient propagation in deep networks through identity shortcut connections. The middle section shows the internal data processing path of the spatial attention module.

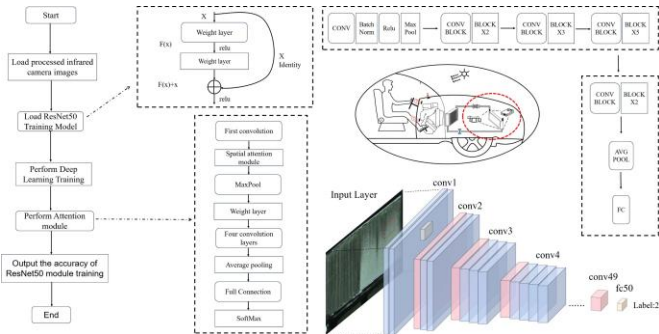


Fig. 3 Schematic diagram of image recognition

The right side presents the complete forward propagation architecture of the network, including the input layer, a feature extraction backbone composed of sequential convolutional blocks (each containing convolution, batch normalization, ReLU activation, and pooling operations), a global average pooling layer, fully connected layers, and a SoftMax classifier that outputs the predicted category. This integrated architecture is designed to achieve high-precision and robust visual recognition of the frost state on the heat exchanger surface. The bottom-right corner of Figure 3 schematically demonstrates how a frost layer image is analyzed to produce a classification label.

3. RESULTS AND DISCUSSION

3.1 Frost layer condition

Figure 4 illustrates the dynamics of frost layer growth on the surface of the outdoor heat exchanger over time (0–12 minutes) under different ambient temperatures (2 °C, 0 °C, –2 °C) and compressor speeds (4000 and 5000 rpm). The results show that higher rotational speeds lead to increased frost formation, as the higher airflow velocity accelerates the condensation of water vapor onto the cooled surface. Additionally, lower ambient temperatures result in more frost accumulation, since colder air causes water vapor to reach the dew point more readily and condense into frost. It was also

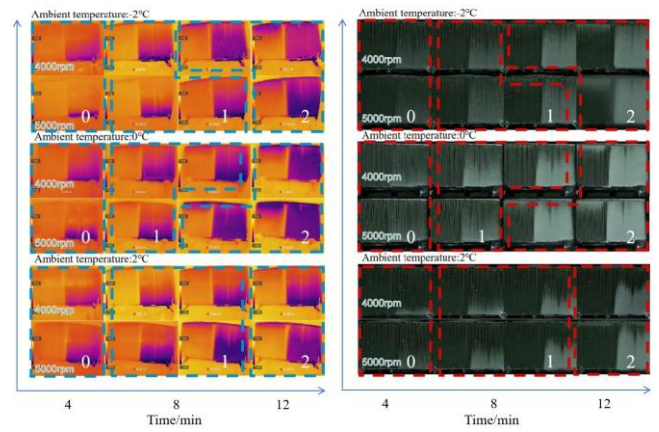


Fig. 4 Frost layer growth diagram

observed that temperature has a greater effect on frost layer growth than compressor speed, primarily because temperature directly determines the conditions for condensation, while compressor speed mainly influences heat exchange efficiency and system pressure variations.

Through multiple sets of parallel curves, the effects of two key factors—ambient temperature and compressor speed—on the frosting process are visually compared. At the same airflow rate, lower ambient temperatures lead to faster frost accumulation and higher frost density. Under the same temperature conditions, higher compressor speeds delay frost thickening by enhancing air convection and may alter the frost crystal structure, resulting in a slightly thinner frost layer at 5000 rpm compared to 4000 rpm.

In this study, the frost growth process is divided into three stages—Initial, Development, and Frosting—corresponding to labels 0, 1, and 2 within the red dashed boxes in the figure. This classification facilitates subsequent image recognition. The figure comprehensively illustrates the sensitivity of frosting behavior to operating conditions, providing key experimental evidence for understanding frost growth mechanisms and optimizing defrosting strategies.

3.2 Frost coverage rate

This study establishes the relationships among system performance, Frost Coverage Rate (FCR), and

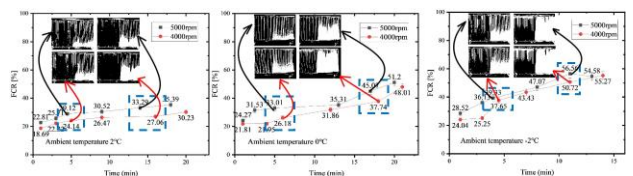


Fig. 5 FCR transformation curve under different operating conditions

image recognition, enabling a comprehensive analysis of the impacts of frost formation.

Figure 5 shows the variation of FCR over time under different ambient temperatures and compressor speeds, along with the corresponding grayscale images for each operating condition.

As shown in Figure 5, FCR increases over time across all tested temperatures. At any given time, the FCR at 5000 rpm is consistently higher than that at 4000 rpm. The blue boxes indicate decision thresholds: 0 to 1 represents the transition from heating mode to eco-defrosting mode, and 1 to 2 represents the transition from eco-defrosting mode to standard defrosting mode. To facilitate interpretation, the grayscale images corresponding to these decision points are included in the figure.

3.3 System performance

Figure 6 illustrates the variations of key system performance parameters over time at different rotational speeds and three ambient temperatures. Compressor suction and discharge temperatures, heating capacity, and COP are critical indicators for evaluating system performance. These parameters are interrelated, and their fluctuations directly impact the operational efficiency of the heat pump air conditioning system.

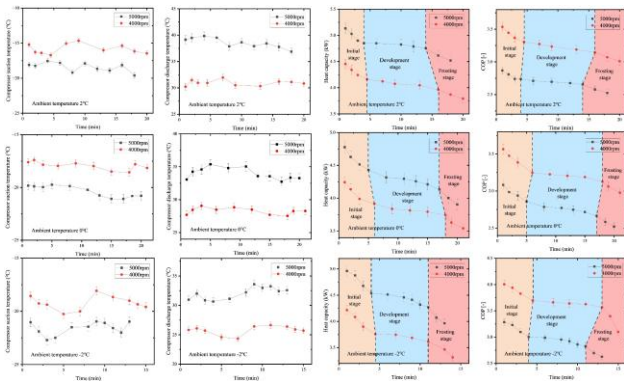


Fig. 6 Frost layer growth diagram

As shown in Figure 6, the compressor suction and discharge temperatures fluctuate around relatively stable values, reflecting the system’s automatic regulation mechanism that maintains operational stability. Higher rotational speeds result in lower discharge temperatures due to reduced heat accumulation and improved heat exchange efficiency during the shortened compression process. Conversely, suction temperatures increase at higher speeds, primarily because the accelerated refrigerant flow limits

precooling time, and the associated lower suction pressure raises the temperature of the incoming refrigerant gas.

In this study, the frost growth process is divided into three stages—Initial, Development, and Frosting—corresponding to labels 0, 1, and 2 within the red dashed boxes in the figure. This classification facilitates subsequent image recognition. The figure clearly illustrates the sensitivity of frosting behavior to operating conditions, providing essential experimental evidence for understanding frost growth mechanisms and optimizing defrosting strategies.

3.4 Image recognition

Figure 7 presents the confusion matrices under different ambient temperatures, along with the corresponding loss and accuracy curves. The confusion matrix enables a detailed evaluation of prediction performance for each class, which is particularly important for handling class imbalance. The loss curve tracks training convergence and helps identify potential overfitting or underfitting, while the accuracy curve provides an intuitive overview of overall model

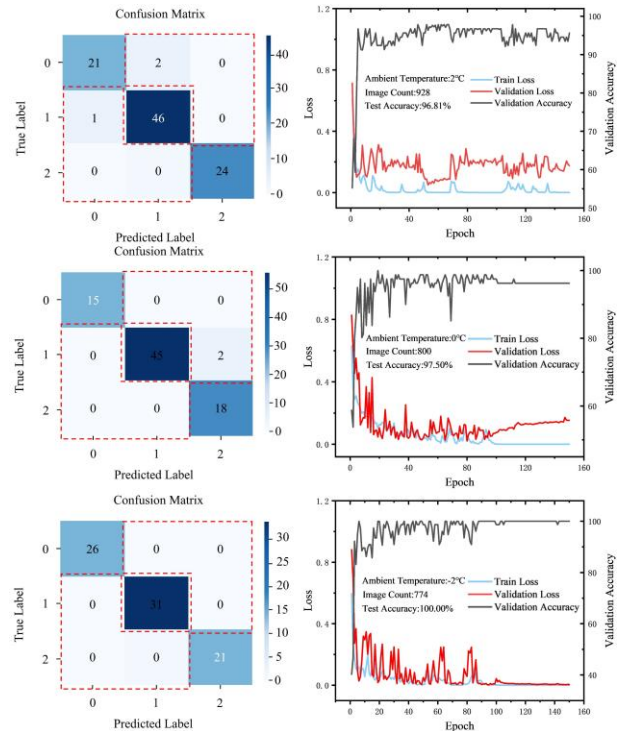


Fig. 7 Frost layer growth diagram

performance and assists in diagnosing fitting issues.

In the confusion matrix, labels 0, 1, and 2 correspond to heat pump mode, eco-defrosting mode, and standard defrosting mode, respectively. The horizontal axis represents predicted labels, and the vertical axis

represents true labels. Values along the diagonal indicate correct predictions, whereas misclassifications are highlighted with red dashed lines. For example, the entry in the first row and second column of the first subfigure shows that when the true label is 0 (heat pump mode), the model predicted label 1 (eco-defrosting mode). The number "2" in this cell reflects the proportion of such misclassifications.

In the loss and accuracy charts, the horizontal axis represents the number of training epochs. The right vertical axis corresponds to the validation accuracy (black curve), while the left vertical axis corresponds to the loss, including the training loss (blue curve) and validation loss (red curve). As shown in Figure 7, accuracy gradually increases and stabilizes with more epochs, while loss decreases and levels off, showing no signs of overfitting or underfitting, which confirms the reliability of the training process.

During the initial phase (approximately the first 20 epochs), significant fluctuations occur due to random parameter initialization. The model was trained for a total of 150 epochs, which helped minimize these fluctuations and promote stable convergence. Additionally, the larger sample sizes at 2 °C (928) and 0 °C (800), compared to -2 °C (774), may include more samples with ambiguous features. Despite some fluctuations in loss, validation accuracy eventually converged to 100 %, indicating thorough feature learning at these temperatures.

4. CONCLUSIONS

In this study, experiments were conducted combining image recognition with an attention mechanism and the defrosting judgment of the R290 secondary-circuit heat pump air conditioning system, along with an analysis of the system's operating parameters. The main research findings are summarized as follows:

(1). The frost process can be divided into three stages according to system performance: a sharp decrease in the Initial stage, a stable Development stage, and a rapid decrease during the Frosting stage.

(2). The results show that, although there were slight differences in image recognition accuracy after 150 training epochs at different temperatures, accuracy remained above 95% in all cases.

ACKNOWLEDGEMENT

This work was financially supported by the National Natural Science Foundation of China (NSFC) (Grant No. 52206016, No. 52276079 and No. 52376012).

REFERENCE

- [1] Ibrahim OAM, Kadhim SAK, Karrar A, Hammoodi, Rashid FLR, Askar AH. Review of hydrocarbon refrigerants as drop-in alternatives to high-GWP refrigerants in VCR systems: The case of R290. *Cleaner Eng Technol.* 2024;23:100825. doi:10.1016/j.clet.2024.100825.
- [2] Bani Issa A, Liang C, Liu H, Groll EA, Ziviani D. Experimental analysis of a liquid-to-liquid two-stage R290 heat pump system for residential cold-climate applications. *Appl Therm Eng.* 2025;278:127223. doi:10.1016/j.applthermaleng.2025.127223.
- [3] Liu N, Li D, He J, Li K, Tian Y, Zhang H. Experimental investigation on frosting performance of a microchannel heat exchanger in heat pump system for electric vehicles. *Appl Therm Eng.* 2024;249:123339. doi:10.1016/j.applthermaleng.2024.123339.
- [4] Mehmood MUI, Rahman HU, Desdemir DB, Lazoglu I. Frost-EffNet: A deep learning model for frost detection in refrigeration systems. *Int J Refrigeration.* 2025;180:416-25. doi:10.1016/j.ijrefrig.2025.09.029.
- [5] Zhu R, Liu M, Wang G, Wang Q, Wu W, Li G, Wang H. ANFIS model for prediction of the frost accumulation on surfaces of finned-tube heat exchanger. *Appl Therm Eng.* 2025;280(3):128388. doi:10.1016/j.applthermaleng.2025.128388.
- [6] Rahman HU, Mehmood MUI, Lazoglu I. A centralized frost detection and estimation scheme for Internet-connected domestic refrigerators. *Int J Refrig.* 2025;169:194-203. doi:10.1016/j.ijrefrig.2024.10.032.
- [7] Zheng H, Ma C, Fu D, Sheng W, Wang R, Chen X, Song M, Dang C. A review of defrosting methods in cold storage. *Renew Sustain Energy Rev.* 2025;214:115553. doi:10.1016/j.rser.2025.115553.
- [8] Braun LPB, Reis RG, Nascimento CAR, Silveira AS, Hermes CJL. Experimental study of the cross-influence of frost morphology and defrost strategy on the performance of tube-fin evaporators of household refrigerators. *Thermo.* 2025;5:32. doi:10.3390/thermo5030032.
- [9] D Y, Wu J, Wang C. Experimental study on dynamic characteristics of an R290 heat pump during defrost. *Energy Build.* 2020;223:110174. doi:10.1016/j.enbuild.2020.110174.
- [10] D Y, Wu J, Wang C, Chen R, Li J. Investigation on the influence of EEV opening on the reliability of an R290 ASHP during defrosting. *Energy Build.* 2020;223:110218.